Incompressible Biventricular Model Construction and Heart Segmentation of 4D Tagged MRI

Albert Montillo[1*,2], Dimitris Metaxas[2], and Leon Axel[3]

[1*] GE Global Research Center, Niskayuna, NY, USA; montillo@ge.com

[2] Department of Computer Science, Rutgers University, Piscataway, NJ, USA

[3] Department of Radiology, New York University Langone Medical Center, New York, NY, USA

Abstract Most automated methods for cardiac segmentation are not directly applicable to tagged MRI (tMRI) because they do not handle all of the analysis challenges: tags obscure heart boundaries, low contrast, image artifacts, and radial image planes. Other methods do not process all acquired tMRI data or do not ensure tissue incompressibility. In this chapter, we present a cardiac segmentation method for tMRI which requires no user input, suppresses image artifacts, extracts heart features using 3D grayscale morphology, and constructs a biventricular model from the data that ensures the near incompressibility of heart tissue. We project landmarks of 3D features along curves in the solution to a PDE, and embed biomechanical constraints using the finite element method. Testing on normal and diseased subjects yields an RMS segmentation accuracy of ∼2 mm, comparing favorably with manual segmentation, interexpert variability and segmentation methods for nontagged cine MRI.

Keywords Incompressible biventricular model · Mesh construction · FEM · tMRI

1 Introduction

In most developed countries, cardiovascular disease kills more men and women than any other disease. An automated characterization of myocardial deformation may lead to improved patient diagnosis and treatment. Tagged MRI (tMRI) [1, 2] induces an intramyocardial magnetic tag (line) pattern throughout the heart and can image the tagged soft heart tissue through bone noninvasively, making it a gold standard for measuring regional myocardial deformation abnormalities. However, tracking the deformation requires the dynamic segmentation of the outer (epicardial) and inner (endocardial) heart boundary surfaces, and tracking the tags.

A. Montillo (✉)

GE Global Research Center, Niskayuna, NY, USA

and

Department of Computer Science, Rutgers University, Piscataway, NJ, USA

e-mail: montillo@ge.com

Dynamic segmentation of these boundary surfaces is important for many reasons. First, it can facilitate a wide variety of tag tracking methods. Tag tracking methods based on tag sheet tracking, including [3–5] optical flow and HARP [3], rely upon manually segmented boundaries to improve performance by restricting the tags tracked to just those within the myocardium. This manual segmentation is tedious and operator dependent. Second, if the boundaries can be segmented, interpolating the 3D motion throughout the myocardium with a finite element method (FEM) model becomes possible, even in thin-walled structures, such as the right ventricle (RV) [3, 7], where there is a sparsity of tags. Third, segmenting the walls also provides a necessary boundary condition to study the distribution of myocardial stress [8]. The fourth reason is that the heart boundaries from tMRI can be used to calculate classical descriptors of heart function at the same accuracy as those obtained through nontagged MRI [9].

The most desirable tMRI segmentation must not only handle the arduous processing challenges specific to tMRI, but also be fully automated, perform 3D biventricular segmentation, and impose the near incompressibility constraint of real myocardial tissue. Full automation is essential to provide the response time and objectivity necessary for routine clinical use. Most previous tMRI segmentation methods are either manually driven or tend to require manual editing, e.g. [4, 10]. More recent methods, e.g. [11–16], have one or more of these limitations: they provide only a 2D analysis [12], segment only one surface of one ventricle [13], or only segment one ventricle and require manually drawn initial contours or landmarks [14–16], or do not impose incompressibility [11]. 3D analysis is required to handle cases in which the heart appears to change topology as portions of the heart move into and out of the 2D image planes. Incompressibility should be imposed to ensure physiologically sound segmentation throughout systole.

Many segmentation methods have been proposed for imaging modalities *other* than tMRI such as cardiac ultrasound, CT, and nontagged cine MRI, including [17–20]. However, segmentation results are *not* shown for tagged MRI, primarily due to the arduous processing challenges of tMRI: (1) image artifacts including intensity inhomogeneity and intersubject intensity variation must be suppressed, (2) tag lines that obscure heart boundaries must be removed, (3) boundary-delineating features must be extracted despite low image contrast, and (4) the inherently 5D data (3D + time + tag line orientations) must be fused into a single coherent interpretation.

Our objective is to develop a method that segments the 3D biventricular myocardium in tMRI throughout the heart's contraction without requiring user input. We construct a *volumetric* biomechanical model with the near incompressibility constraint of real myocardial tissue in order to (1) yield physiologically sound segmentation and (2) so that epicardial (epi) and endocardial (endo) walls do not merge together, a common failure mode that plagues many *surface*-based segmentation methods.

In Sect. 2, we present four steps of our method: (1) image artifact suppression, (2) feature extraction, (3) volumetric biomechanical model construction, and (4) model fitting. We present our segmentation results in Sect. 3 and provide discussion and conclusions in the final section.

2 Methods

Each time frame of our tMRI consists of three sets of image planes: two short axis (SA) sets and one long axis (LA) set. The SA sets differ with tags running in vertical or horizontal directions (Fig. 1a). Several challenges we face are also illustrated: in Fig. 1a, the use of surface coils can cause intrasubject intensity inhomogeneity; in Fig. 1b, images with 1 mm^2 in-plane resolution come in sparse parallel planes with 8 mm spacing and sparse radially planes with 20° separation; and in Fig. 1c, the lack of intrinsic baseline for MR, can cause intersubject intensity variation at the same windowing level.

2.1 Artifact Suppression

Previous intensity inhomogeneity correction methods assume a priori segmentation, intensity distribution, or are not suited for radially arranged images. To solve, we iterate the following steps (Fig. 2) until the set of sampling points is constant: (1) compute scale at every pixel, where scale is defined as the radius of the largest ball, centered at the pixel, for which pixel intensity homogeneity measures are preserved including the pixel intensities and the gradient magnitude of the intensities in the neighborhood around the pixel, (2) find largest connected component with maximum scale, (3) fit a Gaussian to its intensity distribution, and define field sampling points as those with intensities within 1σ of the mean of this Gaussian, (4) estimate inhomogeneity by fitting second degree polynomial to sampling point intensities, and (5) divide current image intensities pixel-wise by inhomogeneity estimate. Step 2 estimates a region likely to belong to the same tissue. To better sample the inhomogeneity, step 3 extends this region to include nonconnected points which have similar intensities. For further details and performance on noncardiac images see [21].

To suppress intersubject variations, previous methods, such as [22] map zero crossings (zc) in a test image to those in a high contrast reference standard image, I_{HC}. However, in tMRI, zero crossings are unreliable, as foreground and background histogram peaks tend to merge (Fig. 3a). To solve, we characterize the cumulative
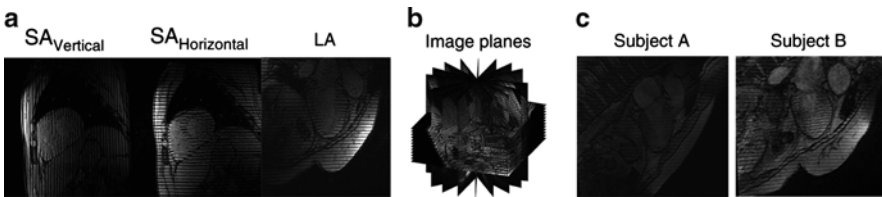

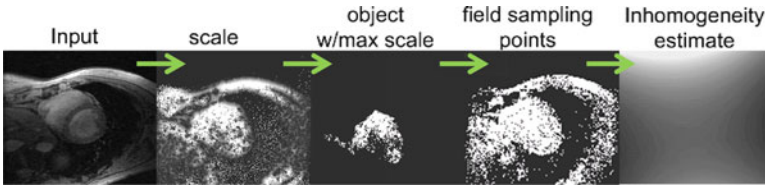**Fig. 1** Raw tMRI: (**a**) 3-tag orientations, (**b**) sparse images, (**c**) intersubject variation

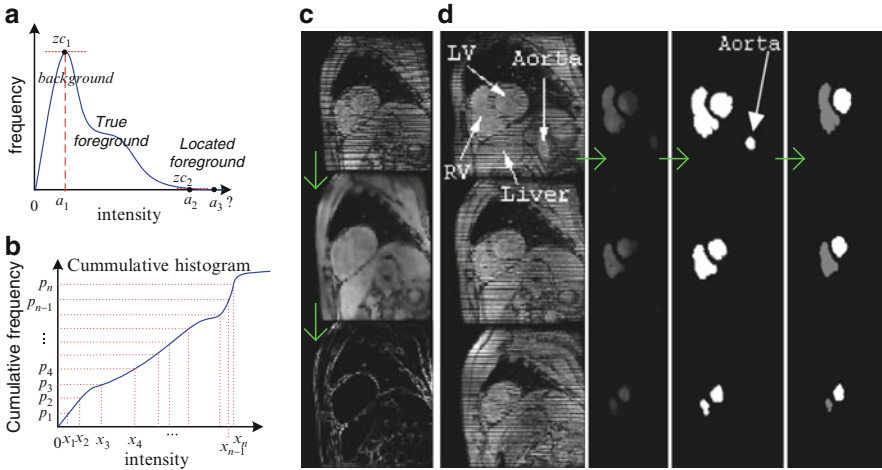**Fig. 2** From left to right, the iterative intensity inhomogeneity correction steps

Fig. 3 (**a**, **b**) Intersubject variation suppresion. (**c**, **d**) Features for epi and endo surfaces

tMRI histogram by its intensities $\widetilde{x}_1, \ldots, \widetilde{x}_{16}$ at a uniform distribution of percentiles, $p_1, \ldots, p_{16}$ (Fig. 3b). We then map original intensities to those of I_{HC} using linear interpolation to make all images have the high contrast of I_{HC}.

2.2 Feature Extraction

Segmenting the biventricular myocardium requires locating the heart and delineating the boundaries of the epicardial surface and the RV and LV endocardial surfaces. To find epicardial boundary features, we perform a grayscale morphological closing with a linear structuring element whose length is equal to tag separation distance, d_{sep} (a known MR pulse sequence parameter), noise suppress, and then perform edge detection (Fig. 3c). To find endocardial boundary features, we observe that the whole image is tagged except for blood because the motion of the blood washes away the tags (Fig. 3d).

Therefore, to isolate blood regions, we apply a 3D grayscale opening operation with a cylinder-shaped structuring element whose radius is $2d_{sep}$ and whose height

spans four parallel image planes. We threshold the output to form blood regions and prune them to just the ventricular blood regions (Fig. 3d, third and fourth columns). We do this by finding the regions with highest spatial–temporal consistency score. This score is measured by the overlap with regions in the same frame but in different image planes through the heart, and in the same image plane but over time. The LV and RV blood is the pair of regions that appears most consistently over space and time.

2.3 Model Construction

2.3.1 Early Systolic Heart Shape Estimate

We form an estimate of the pose, size, and shape of the heart's ventricles by combining the blood region features from the early part of systole, i.e., from the first 1/3 of time frames. In the images of this early part of systole, we automatically determine the most superior SA image to use to form our model, by identifying the most superior SA image for which the RV blood region features found in Sect. 2.2 have not bifurcated into inflow and outflow tracks. We include this image and all inferior images in the following model construction step. For these early systolic images, we interpolate each stack of region features over space using 2.5D shape interpolation [23] which forms a 2.5D distance transform (DT). This is the same pixel from which each SA image is spline interpolated to form intensities between our sparse image planes. We then compute true 3D DTs representing the blood shapes (denoted $\mathbb{D}_{RVB}, \mathbb{D}_{LVB}$) by the Euclidian distance to the zero surface (Fig. 4, step 1). Then we form a robust estimate of the early systolic ventricles by averaging the 3D DTs from both SA tag orientations and all early systolic frames (Fig. 4, step 2).

We form the epicardial surface from two components. The first component, the LV epi surface (zero surface of $\mathbb{D}_{LVEpi}$), is formed by dilating the LV endocardial surface by an estimate of the LV thickness, $\alpha_{LVThickness}$ by subtracting a fixed distance from its 3D (signed) DT representation.This is estimated from the separation of LV and RV endo features. The 2nd component, the RV epi surface, is the zero
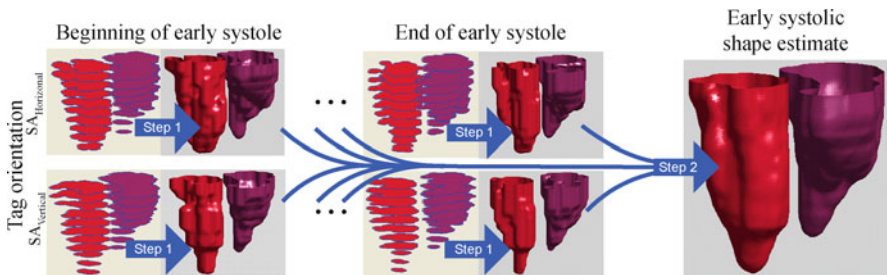

Fig. 4 Region features are fused to form early systolic estimate of endo surface shape
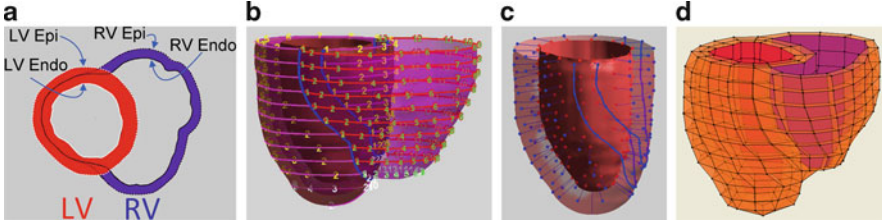
Fig. 5 (**a**) Blood surfaces are joined to form epi surface. Circumferential and longitudinal (**b**) and transmural (**c**) coordinate curves enable mesh construction (**d**)

surface of $\mathbb{D}_{\text{RVEpi}}$ which is formed by combining the dilated RV blood shape, $\mathbb{D}_{\text{RVB}}$, and the LV blood shape, $\mathbb{D}_{\text{LVB}}$, using an energy representation with exponentiation operator:

$$\mathbb{D}_{\text{RVEpi}} = \exp\left(-\frac{\mathbb{D}_{\text{RVB}} - \alpha_{\text{RVThickness}}}{\alpha_{\text{RVThickness}}}\right) + \exp\left(-\frac{\mathbb{D}_{\text{LVB}} - 0.5(\alpha_{\text{LVThickness}})}{1.5(\alpha_{\text{LVThickness}})}\right) \quad (1)$$

where $\alpha_{\text{RVThickness}} = (1/2)\alpha_{\text{LVThickness}}$. This forms a surface surrounding the RV endo as shown in 2D cross-sectional view in Fig. 5a. The portion of this implicit surface outside the LV epi (i.e., $\mathbb{D}_{\text{LVEpi}} > 0$) is retained as RV epi and joined to the LV epi.

2.3.2 Mesh Construction

Constructing a finite element model requires a mesh for the volume between the epicardial surface and endocardial surfaces. To form the mesh we create coordinate curves that map where mesh element vertices will be. Circumferential coordinates are evenly distributed on the combined epi surface according to arc length, starting at the line of insertion (blue) of the RV epi into LV epi as shown in Fig. 5b. Longitudinal coordinates are distributed evenly from apex to base. Transmural coordinates are distributed along curves running from outer to inner wall which are formed by computing the characteristic curves through the solution, $\bar{v}^*$, that minimizes the 3D version of gradient vector flow (GVF) [24] equation:

$$\bar{v}^* = \arg\min_{\bar{v}} E(\bar{v})$$
$$= \arg\min_{\bar{v}} \iiint \mu \left(u_x^2 + u_y^2 + u_z^2 + v_x^2 + v_y^2 + v_z^2 + w_x^2 + w_y^2 + w_z^2\right)$$
$$+ |\nabla f|^2 |(\bar{v} - \nabla f)|^2 \, dx \, dy \, dz \quad (2)$$

where μ balances smoothing and data fidelity. The gradient is taken on the function f which is a discrete grayscale labeled volume with dark intensity pixels outside the heart, medium gray between the walls, and bright white ventricular blood pixels.

For all our subjects, $\mu = 0.15$. To minimize this functional, we use the calculus of variations to derive the necessary condition: $\bar{v}_t = \mu \nabla^2 \bar{v} - |\nabla f|^2 (\bar{v} - \nabla f)$ and iterate until the equilibrium solution, $\bar{v}^*$. Starting from each epicardial node formed along the circumferential directions, we traverse the characteristic curve in $\bar{v}^*$ until we reach an endocardial surface. We then evenly divide each projection curve by arc length. Example characteristic curves are shown as thin blue lines in Fig. 5c for the LV. We also apply this for transmural RV curves. Connecting neighboring points along the coordinate curves forms mesh elements (Fig. 5d).

2.3.3 Biomechanical Model

For segmentation, we model the myocardial tissue as an elastic material character-ized by Young's modulus E, and Poisson ratio, v. We denote the strain-displacement matrix as **B** and the material property matrix as **P**, and use: $\mathbf{K}_{el}(\mathbf{P}(E,v)) = \iiint \mathbf{B}^T\mathbf{P}\mathbf{B}\,dV$ [25] as the formulation of the stiffness matrix for each mesh element. We assemble the global stiffness matrix **K** from K_{el} [26] using the finite element method. Our model's internal forces are then **Kq** where **q** is the vector of mesh nodes positions. As the myocardium is nearly incompressible, we use $v = 0.4$ while we empirically choose $E = 0.1$ megapascals (MPa), a value that provides realistic smoothness for the quality of the images we acquired. The value of E is less critical and can be varied while still producing similar overall segmentation results.

2.4 Fit Model to Dynamically Segment Patient-Specific Anatomy

Image forces guide the fitting of our model to patient anatomy for each frame. Inner walls are attracted to forces from blood features and the outer wall to the edge fea-tures that we extracted in Sect. 2.2 for each image plane. We compute the gradient of these feature images and employ GVF to increase their capture range. We do not apply a 3D gradient operator to an interpolated isotropic voxel volume because the widely spaced image planes make isotropic voxel volumes less representative of anatomy. Instead, we compute the intersection of our model's edges with the image planes. The 2D image force acting on each edge intersection point is affine distributed to the edge's two endpoints (i.e. the model's nodes) based on the dis-tance of the intersection point to each endpoint. This forms our model's external forces, f_{ext}.

We formulate model fitting as force balance equation in which internal and ex-ternal forces compete to explain the data. The motion of model's nodes is governed by a second order Lagrangian equation: $\mathbf{M}\ddot{\mathbf{q}} + \mathbf{D}\dot{\mathbf{q}} + \mathbf{Kq} = f_{ext}$. Setting $\mathbf{M} = 0$ and $\mathbf{D} =$ identity leaves $\dot{\mathbf{q}} + \mathbf{Kq} = f_{ext}$. We solve this with numeric integration, which we iterate until the forces equilibrate or vanish.

To track the heart's shape change throughout systole, we begin by fitting the model to the first frame, t_n, in which the motion of the blood has washed away the

tags. To fit subsequent time frames ($t > t_n$) we propagate the previous frame solution and fit the model in the new frame. To fit earlier time frames, (e.g. t_{n-1}), we propagate the solution from t_n and fit the model but we do not apply forces to the endocardial walls because the insufficient blood–myocardium contrast yields unreliable blood regions features, however, both the epicardial and endocardial surfaces are recovered because of (1) the incompressibility constraint, (2) the equilibrium model fit at t_n, and (3) reliable epicardial features at t_n and t_{n-1}.

3   Results

We acquired tMRI data from ten subjects: eight normal and two with right ventricular hypertrophy. Each sequence contains 12–15 frames; each frame contains three volumes (2D img. sets) with one set in each of three orthogonal tag orientations. In total, we collected 1,160 2D images. Two (2) expert physicians segmented the LV and RV endocardial boundaries, and the epicardial boundary providing the ground truth for evaluation purposes. We form expert surfaces from expert contours using a process similar to the one described in Sect. 2.3 for converting 2D blood region features into 3D surfaces, only now we form 3D distance transforms from stacked expert contoured regions. For each expert, this produces one 3D DT for each of feature (i.e., LV endo, RV endo, and combined LV and RV epi) whose zero isosurface defines an expert surface.

3.1   Artifact Suppression Results

During acquisition, surface coils are placed on the subject's chest, S_c, and back, S_b (Fig. 6a). Coils improve SNR but cause pixels in coil vicinity to be brighter than those in the deep thoracic region, labeled DpTh. When we suppress the intensity inhomogeneity artifact in the raw input tMRI (Fig. 6a, first column) it causes
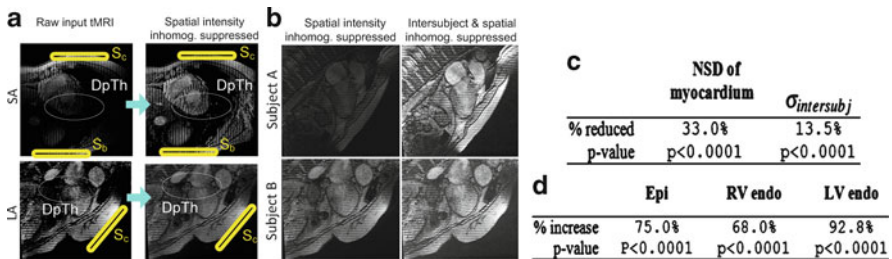

Fig. 6 Examples of intrasubject (**a**) and intersubject (**b**) intensity variation suppression. Database-wide reduction in intensity variations (**c**) also increases (**d**) boundary edge strength

DpTh region contrast to be visibly increased (Fig. 6a, second column). Additionally, MR lacks an intrinsic baseline signal level causing intersubject intensity variations shown in Fig. 6b first column (also Fig. 1c). Our histogram standardization creates more consistent image contrast across subjects (Fig. 6b, second column). Statistical analysis of the 1,160 images (Fig. 6c) shows our intrasubject intensity inhomogeneity suppression yields 33.0% reduction in the normalized standard deviation (NSD) of the (tag removed) myocardial pixel intensities. The intersubject intensity variation suppression yields a 13.5% reduction in the standard deviation of the mean myocardial pixel intensity ($\sigma_{\text{intersubj}}$) across the subjects in our database.

We measured the cumulative effect of our artifact suppression methods by computing the mean magnitude of the image gradient orthogonal to the expert boundaries at points distributed evenly on the boundary. Figure 6d shows our artifact suppression caused all-boundary edge strengths to increase. The epicardial boundary edge strength increased by 75.0%, RV endo by 68%, and LV endo by 92.8%.

3.2 Segmentation Results

Figure 7 is representative of the physiologically sound segmentation from our method. The model's outer surface is transparent here to view the mesh and inner surfaces. The 3D model is intersected by a 2D LA image. From this perspective, we can see (1) the model's near incompressibility constraint maintains sound surface-to-surface separation even of the intervening septal wall and (2) the contraction of the LV endocardial surface from early to end systole (left to right).

Figure 8 shows solid curves for the intersection of our 3D model with an image plane, and dashed curves for the expert's boundaries. Representative results from one subject are shown in (a) and from another subject in (b). High correspondence between segmented and expert boundaries is evident throughout contraction in both the SA and LA images, the latter of which is not handled by other methods such as [12, 27].

We also perform a quantitative validation of our method to measure its accuracy. Specifically, we compute the distance between points on each model surface, (denoted by A), and points on the corresponding expert surface, (denoted by B)
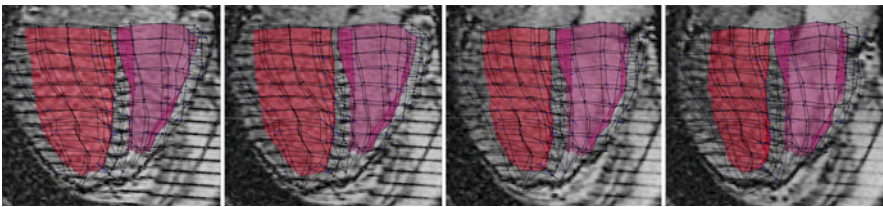

Fig. 7 3D model intersected by images during systole. LV endo (*red*) and RV endo (*purple)*
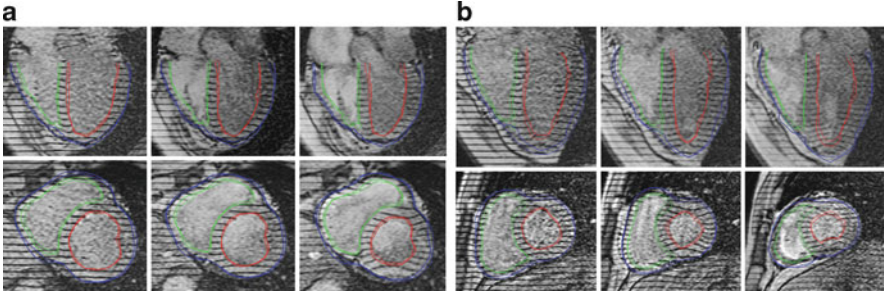
Fig. 8 (**a**) shows the image plane curves in early to end systole (from *left* to *right*), with *green* = RV endo, *red* = LV endo, *blue* = epi. Model (*solid*); experts (*dashed*), (**b**) is another subject

Table 1 Distance errors across subjects, Man = inter-expert, Auto = method-to-expert distance

Error measurement	Method	LV endocardial	RV endocardial	Epicardial	All surfaces
RMS	Man	1.78 ± 0.39	1.88 ± 0.63	1.35 ± 0.54	1.58 ± 0.46
	Auto	2.00 ± 0.41	2.58 ± 0.63	2.51 ± 0.12	2.38 ± 0.36
Median	Man	1.51 ± 0.32	1.41 ± 0.45	1.03 ± 0.48	1.19 ± 0.40
	Auto	1.63 ± 0.26	2.18 ± 0.54	2.06 ± 0.02	1.94 ± 0.25

using: $d(a, \boldsymbol{B}) = \min_{b \in \boldsymbol{B}} \|a - b\|$ for all points a on the model surface. In Table 1, the first error measure is the average root mean squared (RMS) distance across subjects; the second is the average median error across the subjects. For each error measure the first entry (Man) is the distance between the experts' manual delineations, while the second entry (Auto) is the distance between our method and the corresponding expert surface. The errors are computed for each surface and for all surfaces combined. Overall our method's RMS error is only ∼1 mm more than the interexpert distance. Our RMS error varies from 2.0 mm for the LV endo to 2.58 mm for the RV endo. The average median error across subjects is the second entry which is slightly lower than RMS error. Standard deviation is small for all measures, indicating we are consistently locating the boundary surfaces well across the subjects. Previous methods [12, 27] reporting ∼1 mm accuracy require *as input* the expert's contours in the first frame. Our method does not require this input as it solves heart localization automatically as part of the segmentation task.

4 Discussion and Conclusions

It is insightful to compare our method to a single statistical atlas approach. A challenge for our model from data-fusion (MFDF) approach is building adequate acquisition postprocessing to suppress image artifacts, while a challenge for a single statistical atlas is acquiring enough representative data of all patient variations. When the data is of high quality or when image examples are scarce (e.g. due to a substantially new MR pulse sequence, or lack of patients with a particular

condition), MFDF may be preferable. Another potential advantage of MFDF is that it may be applicable to a range of myocardial diseases since the method does *not* depend on the similarity of the test subject to samples in a training dataset. For example, MFDF may be adaptable for congenital heart disease (CHD). In CHD anatomical abnormalities such a hole in the septal wall can occur. In such cases, MFDF may be able to discover the topological variation (i.e., a hole) and construct a patient-specific model. Other methods that impose a defect-free model onto the diseased heart may be less able to segment the boundaries and abnormal motion. In such cases MFDF might be used to seed the statistical atlas with the required training segmentations, and this is an area of future work.

We have chosen not to incorporate muscle fiber orientations into our cardiac model for two reasons. The first is that we use the model for two distinct model fitting phases. In phase 1 we fit the early systolic approximate shape model to the specific patient anatomy in the first systolic frame in which the tags are not visible in the blood. In this case, the model adapts to the patient anatomy from an average and adding fiber orientations may over constrain. In phase 2, the model is propagated to earlier and later time frames. Here, it may make sense to add fiber orientations to further regularize, however, most clinics are currently not equipped to acquire patient-specific fiber orientation data in vivo, and assuming a standard orientation may add bias.

Our successful segmentation of low blood–myocardium contrast tMRI with spatially sparse 2D image samples suggests good potential applicability to segment higher contrast SSFP tMRI [28] and densely sampled true 3D tMRI [29]. In addition, our method is likely adaptable to still other types of tMRI. For example, for 2D grid tagging, our blood feature extraction (the most critical task) should work well since there are fewer bright pixels to suppress with the morphological opening. Epicardial features may be extracted, in part, through a slight modification: applying a closing with two orthogonal linear structuring elements and is a topic for future testing. Also, our method does not require perfect intersection of LA image planes; as long as the pose of each image plane is provided, then our region and edge features can be added to the overall set of features that guide modeling fitting.

There are several limitations of our method which are areas for our future work. First, our incompressible model does not yet follow the longitudinal descent of the valves toward the apex. For this, tag motion in LA images might be used to further guide model fitting. Second, the problem of papillary muscles is not fully addressed. We have chosen to include the parts of the papillary muscles that are clearly visible in tMRI (the papillary buds) with the myocardium. This was done for two reasons: (a) we are now in good position to exploit motion data visible from the papillary tags for future 3D motion recovery and (b) we do introduce additional uncertainty. Third, there are artifacts which we do not yet handle including (a) RF interference, (b) images that self-overlap (wrap-around) from aliasing, and (c) distortion from metal implants. The second and third artifacts can make the images difficult to interpret even by expert radiologists. Fourth, "slice misalignment" can be caused by respiratory-induced heart motion. Suppression methods proposed in the literature include breath-hold acquisition, respiratory gating, slice-following, and true 3D

MRI. Breath-hold and respiratory gating are the methods we use. However, breath-hold is not viable for some subject and respiratory gating can lengthen scan time. True 3D MRI is promising but requires the most advanced acquisition hardware and pulse sequences. If none of the methods for mitigating slice misalignment are available another motion correction is required and this remains an open research problem. Lastly, many methods do not attempt to segment either the apex of the LV or RV [12,13,20,27]. Our method attempts both, and does a good job at segmenting the LV apex but tends to truncate the RV apex. Causes include (1) our data samples the LV more densely than the RV, (2) RV apex tends to be narrower, (3) in some cases, RV apex is smaller than the opening structure element which works well to locate the remainder of the RV blood. Future work includes refining the features from this region.

In conclusion, we have presented a MFDF-based biventricular segmentation of the full complement of tMRI data, which required no user input. The model fitting consumes <3 min of CPU time to fit all frames on a dual core desktop, and obviates the interactive contouring task that requires up to 3 h/subject.

References

1. Axel L, Dougherty L. Heart wall motion: improved method of spatial modulation of magnetization for MR imaging. Radiology. 1989;172:349–350.
2. Zerhouni E, Parish D, Rogers W, Yang A, Shapiro E. Human heart: tagging with MR imaging-a method for non-invasive assessment of myocardial motion. Radiology. 1988;169:59–63.
3. Haber I, Metaxas D, Axel L. Three-dimensional motion reconstruction and analysis of the right ventricle using tagged MRI. Med Image Anal. 2000;4(4):335–355.
4. Tustison N, Amini A. Myocardial kinematics based on tagged MRI from volumetric NURBS models. In: SPIE. vol. 5369; 2003.
5. Young A, Axel L. Three-dimensional motion and deformation of the heart wall: estimation with spatial modulation of magnetization–a model-based approach. Radiology. 1992;185:241–247.
6. Osman N, Prince J. Angle images for measuring heart motion from tagged MRI. In: ICIP; 1998. p.704–8.
7. Young A, Fayad Z, Axel L. Right ventricular midwall surface motion and deformation using magnetic resonance tagging. Am J Physiol. 1996;271:H2677–H2688.
8. Hu Z, Metaxas D, Axel L. In vivo strain and stress estimation of the heart left and right ventricles from MRI images. Med Image Anal. 2003;7(4):435–444.
9. Dornier C, Ivancevic M, Lecoq G, Osman N, Foxall D, Righetti A, et al. Assessment of the left ventricle ejection fraction by MRI tagging. In: ISMRM; 2002.
10. Guttman M, Prince J, McVeigh E. Tag and Contour Detection in Tagged MR Images of the Left Ventricle. IEEE Trans Med Imaging. 1994;13(1):74–88.
11. Montillo A, Metaxas D, Axel L. Automated deformable model-based segmentation of the left and right ventricles in tagged cardiac MRI. In: MICCAI; 2003. p. 507–515.
12. Qian Z, Metaxas D, Axel L. Boosting and nonparametric based tracking of tagged MRI cardiac boundaries. In: MICCAI; 2006. p. 636–644.
13. Huang J, Huang X, Metaxas D, Axel L. Adaptive Metamorphs Model for 3D Medical Image Segmentation. In: MICCAI; 2007.
14. Sundar H, Davatzikos C, Biros G. Biomechanically-Constrained 4D Estimation of Myocardial Motion. In: MICCAI; 2009.
15. Chandrashekara R, Mohiaddin R, Razavi R, Rueckert D. Nonrigid Image Registration with Subdivision Lattices: Application to Cardiac MR Image Analysis. In: MICCAI; 2007.

16. Zhang S, Wang X, Metaxas D, Chen T, Axel L. LV surface reconstruction from sparse tMRI using laplacian surface deformation and optimization. In: ISBI; 2009. p. 698–701.
17. Yang L, Georgescu B, Zheng Y, Meer P, Comaniciu D. 3D ultrasound tracking of the left ventricle using one-step forward prediction and data fusion of collaborative trackers. In: CVPR; 2008.
18. Zhu Y, Papademetris X, Sinusas A, Duncan JS. Segmentation of myocardial volumes from real-time 3D echocardiography using an incompressibility constraint. MICCAI. 2007;10(Pt 1): 44–51.
19. Ecabert O, Peters J, Schramm H, Lorenz C, Von Berg J, Walker MJ, et al. Automatic model-based segmentation of the heart in CT images. IEEE Trans Med Imaging. 2008; 27(9):1189–1202.
20. Bistoquet A, Oshinski J, Skrinjar O. Myocardial deformation recovery from cine MRI using a nearly incompressible biventricular model. Med Image Anal. 2008;12(1):69–85.
21. Zhuge Y, Udupa J, Liu J, Saha P, Iwanaga T. A Scale-Based Method for Correcting Background Intensity Variation in Acquired Images. In: SPIE; 2002. p. 1103–1111.
22. Nyul L, Udupa J, Zhang X. New variants of a method of MRI scale standardization. IEEE Trans Med Imaging. 2000;19(2):143–150.
23. Herman G, Zheng J, Bucholtz C. Shape-based interpolation. IEEE Comput Graph. 1992;p. 69–80.
24. Xu C, Prince J. Generalized Gradient Vector Flow external forces for active contours. Sig Proc. 1998;71:131–9.
25. Cook R, Malkus D, M P. Concepts and applications of finite element analysis. Wiley; 1989.
26. Macneal R. Finite Elements: Their Design and Performance. Marcel Dekker; 1994.
27. Qian Z, Metaxas D, Axel L. Learning methods in segmentation of tMRI. ISBI; 2007. p. 688–691.
28. Herzka D, Guttman M, McVeigh E. Myocardial tagging with SSFP. Magn Reson Med. 2003;49(6):329–340.
29. Ryf S, Spiegel MA, Gerber M, Boesiger P. Myocardial tagging with 3D-CSPAMM. J of Mag Res Imaging. 2002;16:320–325.